# Unraveling the Deformation and Water Storage Characteristics of Different Aquifer Groups by Integrating PS-InSAR Technology and a Spatial Correlation Model

Danni Zhao, Beibei Chen, Huili Gong, Kunchao Lei, Chaofan Zhou, and Jinming Hu

***Abstract*—Land subsidence is an environmental geological phenomenon mainly caused by groundwater overexploitation. Long-term overexploitation of groundwater not only causes compaction of aquifer thickness and surface deformation but also leads to the loss of aquifer water storage capacity. The skeleton water storage coefficient ($S_k$) is an important parameter for evaluating the water storage capacity of aquifer groups. This article proposes a new research framework for obtaining the $S_k$ of different aquifer groups: combining permanent scatter for SAR interferometry technology and a multiscale geographic weighted regression model to obtain subsidence information for different aquifer groups, inverting the $S_k$ of different aquifer groups from the spatial scale, and discussing the deformation characteristics of soil layers under different water head change modes to evaluate the deformation and water storage characteristics of different aquifer groups. This framework is applied to the land subsidence region of the Beijing Plain. We calculated that the settlement proportions of different compression layer groups were 14.75%, 23.65%, 33.44%, and 28.16%. Due to the different lithological compositions and groundwater exploitation of different aquifers, the $S_k$ values exhibit different spatial distribution characteristics. With the continuous development of subsidence, the water storage performance of the aquifer group is continuously declining. These findings contribute to managing the sustainable use of groundwater resources and controlling subsidence. It is demonstrated that the research framework proposed in this article can serve as an effective tool for obtaining settlement information and the $S_k$ of different aquifer groups.**

***Index Terms*—Interferometric synthetic aperture radar (InSAR), land subsidence, multiscale geographically weighted regression (MGWR), stratified skeletal storage coefficient.**

Manuscript received 24 May 2023; revised 17 July 2023, 18 August 2023, 9 September 2023, and 26 September 2023; accepted 8 October 2023. Date of publication 11 October 2023; date of current version 8 January 2024. This work was supported in part by the Beijing Outstanding Young Scientist Program under Grant BJJWZYJH01201910028032, in part by the National Natural Science Foundation of China under Grant 41930109/ D010702, 42371089/ D0104, 42371081/D0104 and Grant 42201081/ D0104. *(Corresponding author: Beibei Chen.)*

Danni Zhao, Beibei Chen, Huili Gong, Chaofan Zhou, and Jinming Hu are with the Key Laboratory of the Ministry of Education Land Subsidence Mechanism and Prevention, Capital Normal University, Beijing 100048, China (e-mail: 2210902146@cnu.edu.cn; 6183@cnu.edu.cn; gonghl@cnu.edu.cn; 6843@cnu.edu.cn; 2200902157@cnu.edu.cn).

Kunchao Lei is with the Beijing Institute of Geo-Environment Monitoring, Beijing 100195, China (e-mail: lkc@bjswd.com).

Digital Object Identifier 10.1109/JSTARS.2023.3323699

## I. Introduction

LAND subsidence is the phenomenon of a decrease in surface altitude within a definite range of the surface. This phenomenon is a slowly changing geological hazard, which is mainly due to excessive groundwater exploitation, resulting in groundwater level reduction, pore-water pressure decline, and effective stress increase. Compressible strata are compressed under the effect of the continuous increase in the effective stress, resulting in land subsidence. Once land subsidence forms, it is difficult to recover. When severe land subsidence occurs in densely populated areas, it will seriously threaten the safety of urban infrastructure, houses, and other facilities. In addition, when the extraction rate of groundwater exceeds its recovery capacity, it can also cause permanent loss of aquifer storage capacity, which is not conducive to the sustainable utilization of water resources. At present, land subsidence is a global geological environmental issue, occurring at varying levels worldwide and affecting countries such as Mexico, Japan, Italy, Iran, and China [1], [2], [3], [4], [5].

Beijing is the capital of China. Since the 1950s, regional land subsidence has rapidly developed owing to permanent overexploitation of groundwater [6], [7], [8]. Therefore, monitoring the development of regional land subsidence, identifying the deformation characteristics of different soil masses under various water head variation modes, clarifying the correlation between water head changes in different aquifers and land subsidence, and exploring the water storage characteristics of different aquifer groups are necessary steps for regional land subsidence prevention and control and water resource management.

The interferometric synthetic aperture radar (InSAR) method can obtain the microwave reflection intensity and phase information of the surface simultaneously. Compared with traditional measurement technology, InSAR technology exhibits all-weather characteristics and a wide measurement range and can achieve large-scale surface deformation monitoring [9]. The persistent scatter InSAR (PS-InSAR) method can overcome the impact of spatiotemporal incoherence on the deformation monitoring accuracy [10]. This technique only identifies and extracts PS points with high coherence and reflectivity in the image, obtains more accurate phase information of PS points, and then conducts accurate phase modeling and deformation

calculations for the whole-scene image to correct for the influence of atmospheric and spatiotemporal incoherence [11]. Therefore, we used time-series PS-InSAR technology to obtain land subsidence information.

Several methods have been developed to simulate and predict land subsidence. There are models based on Terzaghi theory, Biot theory, experiences, and artificial intelligence methods [12], [13]. The most widely used model is the "aquifer drainage" model based on Terzaghi's principle [14]. These models require input of elastic and inelastic skeleton water storage coefficients. The conventional methods used to determine aquifer parameters involve laboratory experiments or pumping experiments. However, it is difficult to obtain undisturbed soil samples from deep layers for experimentation. Therefore, the reliability of the model output and the accuracy of land subsidence prediction cannot be guaranteed. In addition, these parameters can be used to evaluate the water storage capacity of aquifers and estimate the loss of groundwater reserves caused by overexploitation.

Recently, these parameters were obtained through long-term deformation or settlement data obtained from time-series InSAR. The time-series InSAR technique is also applied to many aspects of hydrogeological research: estimating the system characteristics of aquifers (water storage coefficient, conductivity, etc.) [15], [16], [17], [18], [19], [20], evaluating the change in groundwater reserves [21], predicting changes in groundwater head [22], and calibrating mathematical models of groundwater flow [14], [23]. Many studies have applied time-series InSAR technology to aquifer water storage coefficient inversion. For example, the water storage coefficient is estimated according to the inverse slope of the curve by generating a stress–strain curve diagram [23]. Combining InSAR and groundwater head data, the harmonic sequence method was employed to determine the water storage coefficient through linear regression [19]. The multichannel singular spectrum analysis method was used to separate seasonal settlement and seasonal water level change, and ordinary least squares were used to obtain the water storage coefficient considering the lag [24]. However, in most previous studies, the aquifer group was regarded as a whole, without considering the characteristics of different layers in complex aquifer systems. The exploitation of each aquifer layer varies, and the compression of each aquifer group varies. Therefore, we must understand the deformation and water storage characteristics of different aquifer groups. For example, fast independent component analysis and the variable preconsolidation head decomposition method were combined to determine the water storage coefficient of different aquifer groups [25]. Extensometer deformation data were used to estimate the water storage coefficient of different aquifer groups in the Beijing Plain based on preconsolidation water head judgment [26]. However, due to the high cost of layered standards and insufficient monitoring points, this method of using extensometer deformation data combined with water head data for water storage coefficient calculation can only reflect the water storage coefficient of individual points, but it cannot determine the overall regional characteristics. Therefore, this article proposes a new research framework: based on the acquisition of regional land subsidence information using the PS-InSAR monitoring method, the multiscale geographically weighted regression (MGWR) model was applied to investigate the correlation between land subsidence and the water level change in different aquifer groups and quantify the contribution rate of the groundwater head variation in different aquifer groups to regional land subsidence. Based on this contribution rate, layered land subsidence information is obtained. To further explore the deformation characteristics of different layers of soil mass under different water head variation modes, the $S_{ke}$ and $S_{kv}$ of the different aquifer groups in the Beijing land subsidence area were inverted. The deformation and water storage characteristics of the different aquifer groups were evaluated. This study could provide technical support for regional groundwater resource management and precise land subsidence prevention and control.

The rest of this article is organized as follows. Section II describes the research area and its geological conditions and introduces the dataset used. Section III presents the process of PS-InSAR technology. In Section IV, based on the analysis results, the soil deformation characteristics in different settlement areas are analyzed. In Section V, the water storage coefficient of the different aquifer groups is obtained, and the relationship between the water storage coefficient and the depth and lithology is explained. Finally, Section VI concludes this article.

## II. Study Area and Datasets

### A. Description of the Study Area

Beijing is in the northwestern part of the North China Plain, with its center at 116°20'E and 39°56'N. The western and northern parts are mountainous areas, and the southeast is a plain that slopes gently toward the Bohai Sea. The main settlement area is situated in the southeastern plain area, which is mainly composed of the alluvial fan group of the water system. Most of these rivers originate from the northwest mountains, meander through the plains, and flow southeast, ultimately flowing into the Bohai Sea. Many rocks are exposed at the surface in the western and northwestern mountainous areas of Beijing, while the plain area is covered with unconsolidated Quaternary sediments, largely comprising fine silt and sand, with high porosity. This type of terrain is generally prone to settlement (see Fig. 1).

The complex aquifer system gradually transitioned from a single aquifer to multiple aquifers from northwest to southeast across the Beijing Plain. According to research by the Beijing Geological Department, the aquifer system is vertically divided into four aquifer groups (Table I) based on the distribution boundaries of these groups [see Fig. 2(a)] [27]. The phreatic water zone is distributed throughout the whole plain area with a buried depth of approximately 50 m. The lithology mainly includes silt, silty sand, and sandy clay. The groundwater in this layer is supplied by atmospheric precipitation, field irrigation infiltration, and stream infiltration. The distribution area of the first confined aquifer is slightly smaller than the phreatic water area, with a buried depth of 80–100 m. The lithology largely comprises various types of gravel, sand, and clay, belonging to shallow confined water, which is mainly

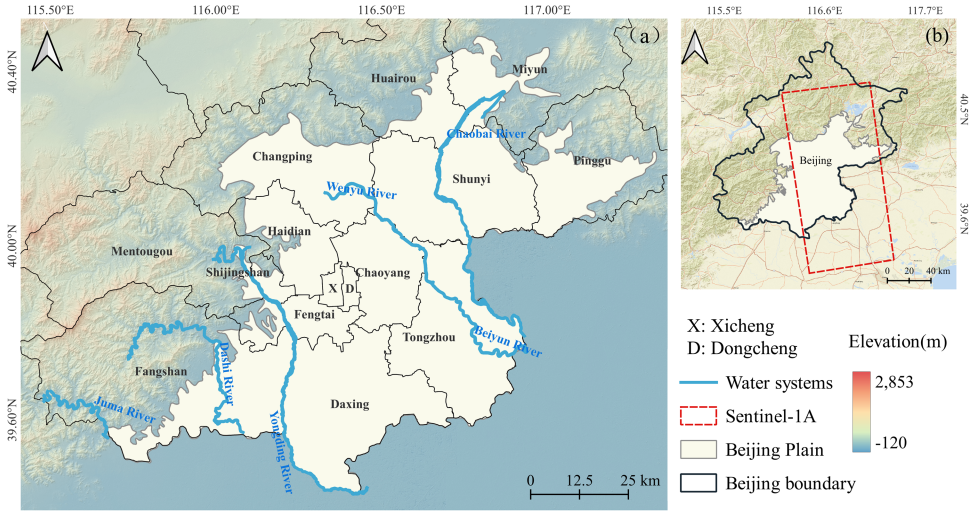


Fig. 1. (a) Distribution map of the five major water systems in the Beijing Plain area. (b) Image coverage map of Sentinel-1A data in Beijing.

TABLE I
DIVISION OF THE AQUIFER GROUPS IN THE BEIJING PLAIN

| Aquifer group | Major lithology | Depth of the bottom (m) |
|---|---|---|
| **Unconfined aquifer (UA)** | Silt, silty sand, and sandy clay | 0–50 |
| **First confined aquifer (FCA)** | Multiple types of gravel, sand, and clay soil | 80–100 |
| **Second confined aquifer (SCA)** | Multiple types of gravel, sand, and clay soil | 100–180 |
| **Third confined aquifer (TCA)** | Mainly sand | 180–300 |

used for agricultural exploitation. The distribution areas of the second and third confined aquifers decrease in turn, with burial depths ranging from 100 to 180 m and 180 to 300 m, respectively. The lithology of the second confined aquifer mainly includes various types of gravel, sand, and clay, belonging to medium-deep confined water, which is mostly used for industrial and domestic exploitation. The lithology of the third confined aquifer primarily comprises sand, belonging to deep confined water, and a small amount is used for industrial and domestic exploitation.

In this article, we used a 1 × 1 km grid to divide the study area, and we covered most land subsidence areas, such as the Chaoyang, Shunyi, Tongzhou, and Daxing districts.

### B. Datasets

A Sentinel-1A satellite dataset from January 2018 to August 2021 was used to obtain land subsidence information (Table II). The external digital elevation model (DEM) data provided by NASA for the 30 m resolution Shuttle Radar Terrain Observation Mission (SRTM) were used for terrain phase removal.

Groundwater data from January 2018 to August 2021 were obtained from the China Geological and Environmental Monitoring Department. According to Section II, we divided the monitoring data of water wells in Beijing into four aquifer groups: UA, FCA, SCA, and TCA (see Fig. 3). Inverse distance weight interpolation based on the well data of each layer was used to obtain the spatial distribution of groundwater changes in different aquifer groups.

To stack the land subsidence results, we used a 1 × 1 km grid to divide the research area in the eastern part of the Beijing Plain, covering most of the land subsidence areas, such as Chaoyang, Shunyi, Tongzhou, and Daxing. The maximum groundwater variation in these areas occurs in the SCA.

TABLE II
SENTINEL-1A PARAMETERS

| Main indicators | Parameter information |
|---|---|
| Flight platform | Sentinel-1A |
| Orbital direction | Ascending |
| Imaging mode | IW |
| Polarization mode | Vertical–vertical (VV) |
| Resolving power | 20×5 m |
| Wavelength | C (0.055466) |
| Return visit cycle | 12 d |
| Angle of incidence | 43.7511° |
| Number of images | 67 |
| Coverage period | January 2018–August 2021 |
| Main image time | 11 January 2021 |

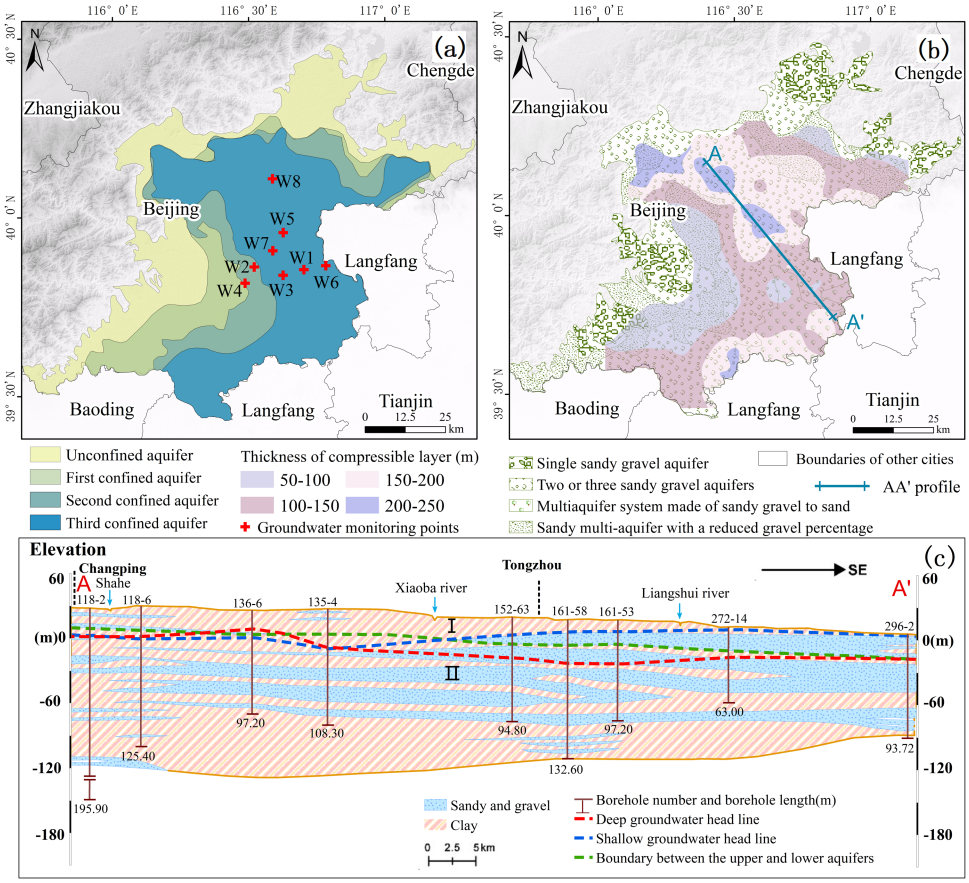


Fig. 2. (a) Distribution of the aquifer groups and groundwater head monitoring points in the Beijing Plain. (b) Characteristics of the aquifer and thickness distribution of the compressible layer. (c) Hydrogeological profile map of the Changping-Tongzhou district (AA′ profile).

## III. Methodology

In this article, a research framework was established and applied to the land subsidence area in Beijing to analyze the deformation and water storage characteristics of the different aquifer groups (see Fig. 4).

1) The PS-InSAR monitoring method was used to obtain deformation information.
2) According to the MGWR method, the spatial distribution of the regression coefficient between the water head variation in the different aquifer groups and land subsidence was analyzed, and then the contribution rate of water head variation in the different aquifer groups to land subsidence was calculated.
3) Combined with the PS-InSAR results and groundwater head data, according to the contribution rate of the groundwater head change in the different aquifer groups to land subsidence, the deformation characteristics of the soil mass were investigated under various water head variation modes, and the $S_k$ of the different aquifers was spatially determined via inversion.

As shown in Fig. 4, 67 Sentinel-1A satellite images within the Beijing Plain area were selected, the PS-InSAR method was adopted to obtain land subsidence information from 2018 to 2021, and then the land subsidence results and groundwater head change information were used to first perform Moran's I analysis to verify whether spatial autocorrelation existed in the water head variation data of the different aquifer groups and the land subsidence data to ensure that the regression model could be further established. Based on this, MGWR2.2 software was used to establish local regression models, namely MGWR models. According to the MGWR model, the spatial distribution of the regression coefficient between the water head variation in the different aquifer groups and land subsidence was analyzed, and the contribution rate of the water head change in the different aquifer groups to land subsidence was determined. Finally, the settlement proportions of different compression layer groups are verified with extensometer data. By combining InSAR and groundwater head change data, the land subsidence data for different aquifers were obtained, the deformation characteristics of the soil layer under different water head variation modes were assessed, the water storage coefficient of the different aquifers was retrieved, and the water storage characteristics of the different aquifer groups were evaluated.

### A. PS-InSAR Processing

Ferretti [28] proposed the PS-InSAR method. It can extract target points with high and stable radiation energy and obtain surface deformation by segregating the terrain phase of the

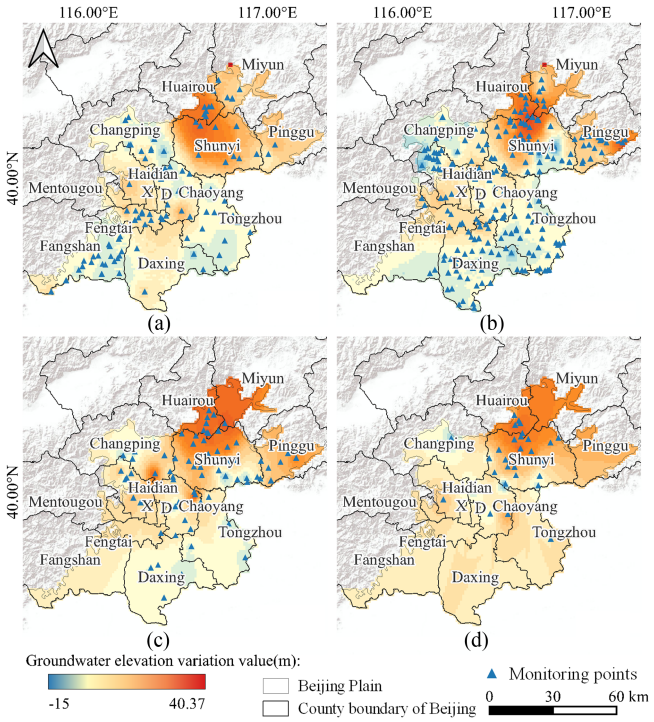


Fig. 3. Spatial distribution map of groundwater level elevation changes and monitoring wells. Spatial distribution map of (a) UA, (b) FCA, (c) SCA, and (d) TCA groundwater elevation changes and monitoring wells.

ground targets. This technology is mature and easy to implement and has good application effects in urban areas such as Beijing.

In this article, SARProZ software [29] was applied to process the 67 Sentinel-1A images of the research area using the PS-InSAR method to obtain relevant deformation information. Among the 67 selected SAR images, one was employed as the main image, and the remaining images were regarded as secondary images. Each secondary image was matched with the main image for interference processing. By introducing external SRTM data as reference DEM data, the topography phase could be removed, and 66 interference phase images could be obtained after interference processing. The interference phase can be decomposed according to the following formula:

$$\Delta \emptyset_{int} = \emptyset_{topo} + \emptyset_{flat} + \emptyset_{def} + \emptyset_{atmos} + \emptyset_{noise} \quad (1)$$

where $\Delta\emptyset_{\text{int}}$ is the interference phase and $\emptyset_{\text{flat}}$ is the flat phase, which was removed using satellite precise orbit data when entering the SAR data. $\emptyset_{\text{topo}}$ is the terrain phase caused by the terrain relief, which is removed via the external DEM data. $\emptyset_{\text{def}}$ is the deformation phase caused by ground displacement during image acquisition. $\emptyset_{\text{atmos}}$ is the atmospheric phase generated by the atmospheric composition. The processing of the acoustic positioning system (APS) in SARProZ software can dispel this phase. $\emptyset_{\text{noise}}$ is the thermal noise and registration error in APS processing, which can be eliminated by using a linear model. When other phase differences are subtracted, the deformed phase $\emptyset_{\text{def}}$ along the line of sight (LOS) direction can be achieved.

InSAR is a side view observation technique that decomposes the LOS deformation results into vertical, east–west, and north–south components. GPS survey results in North China show that the horizontal deformation rate in this area is low, approximately 1.57–1.93 mm/yr [30]. Therefore, the horizontal deformation component was ignored in this study. We converted the deformed phase along the direction of the radar LOS into the vertical displacement ($d_v$) via the following formula:

$$d_v = d_{los} / \cos\theta \quad (2)$$

where $\mathrm{d_{los}}$ is the deformed phase along the radar LOS direction, $\mathrm{d_v}$ is the vertical deformation, and $\theta$ is the incidence angle.

### *B. Correlation Between the Water Head Variation in the Different Aquifer Groups and Land Subsidence*

Moran's I analysis was conducted to verify whether there existed spatial autocorrelation in the water level change data of the different aquifer groups and the land subsidence data to ensure that the regression model could be further established.

Based on this, the MGWR model was established. Compared with the GWR method, the MGWR (3) method relaxes the assumption that all processes to be modeled must be on the same spatial scale and allows each independent variable to have its own different spatial smoothing levels, solving the defect of the GWR model where all variables have the same smoothing level and reducing estimation error [31].

$$y_i = \sum_{j=0}^{k} \beta_{bwj}(u_i, v_i)\, x_{ij} + \varepsilon_i \quad (3)$$

where $(\mathrm{u_i}, \mathrm{v_i})$ denotes the coordinates of the ith sampling point, $x_{ij}$ is the jth prediction variable, $\beta_{bwj}(u_i, v_i)$ is the regression coefficient of the *j*th variable at sampling point i, and $\varepsilon_i$ is the stochastic error at sampling point i. In this article, we used the quadratic kernel function and the Akaike information criterion to determine the kernel function and optimal bandwidth, respectively, of the MGWR model.

### *C. Calculation of the Contribution Rate of Different Aquifer Groups*

In areas with severe subsidence, the correlation coefficient between each grid of different aquifer groups and land subsidence obtained from the MGWR model is used to estimate the contribution rate of the different aquifer groups to land subsidence via the following formula:

$$R_i = \frac{x_i}{\sum_{i=1}^{n} x_i} \quad (4)$$

where $i$ is the ith aquifer, $R_i$ is the contribution rate of the *i*th aquifer group to land subsidence, $n$ is the number of aquifers, and $x_i$ is the sum of all regression coefficients in the grid of areas with severe settlement.

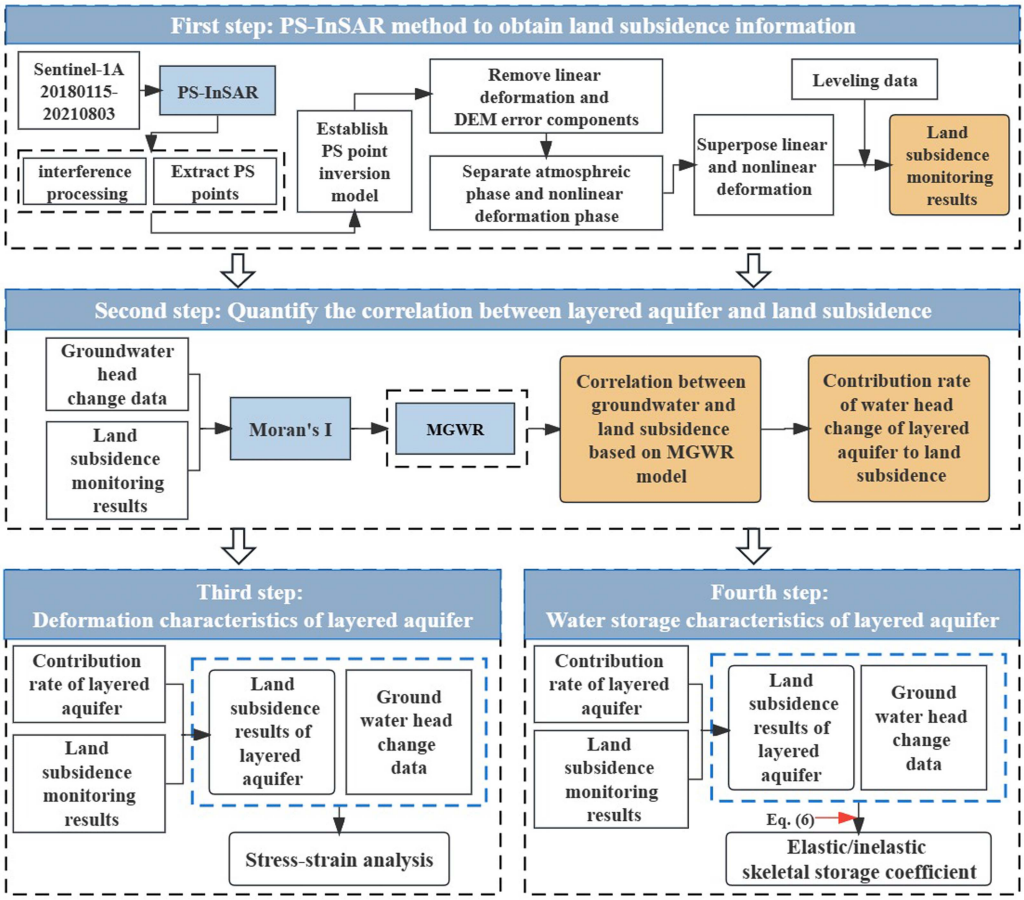


Fig. 4. Flow chart of research methods.

### D. Estimation of the Water Skeletal Storage Coefficient of the Aquifer

The water storage coefficient is an important parameter used to describe the characteristics of aquifers. The specific storage S of a confined aquifer is the amount of water exhausted from the compressible aquifer per unit of aquifer volume under the condition of a unit head decrease [32], [33]. The formula can be expressed as follows:

$$S = \rho g\,(\alpha + n\beta) \tag{5}$$

where $\rho$ is the density of water, g is the gravitational acceleration, $n$ is the void ratio, and $\beta$ is the compressibility of water. $\alpha$ is the compressibility of the volumetric aquifer. Generally, the compressibility of water is much lower than that of aquifer systems. Assuming that the compressibility of water is neglected, $S_k$ is the skeleton water storage related to the compressibility of the aquifer system, which can be determined according to the relationship between the compressibility of the aquifer system and the level variation [34].

$$S_k = \frac{\Delta b}{\Delta h} = S_s\, b_0 \tag{6}$$

where $b_0$ is the initial thickness of the aquifer system, $\Delta h$ is the variation in the water level, $\Delta b$ is the systematic settlement of the aquifer, and $S_s$ is the specific storage.

## IV. Results

### A. InSAR Result Analysis

*1) Leveling Surveying:* To ensure the accuracy of the InSAR land subsidence data, 9 leveling data points (2020–2021) on the Beijing Plain were selected for verification. By establishing a buffer zone with a radius of 100 m centered on every leveling point, the stable coherent points were screened to obtain the average InSAR vertical deformation results within the buffer zone. Then, the goodness of fit $R^2$ was calculated for the leveling data and the mean value. The closer the $R^2$ value was to 1, the better the fitting degree of the regression line to the observed value. The results indicated that the difference between the subsidence monitoring values of the two methods ranged from −9.4 to 8.9 mm, and the average value was 2.3 mm. The distribution trend exhibited satisfactory agreement, and the monitoring values of the two methods were highly correlated, exhibiting a linear regression result of 0.8248 (see Fig. 5).

*2) Land Subsidence Results:* The land subsidence results obtained by PS-InSAR technology are generally relative. This article takes the points in the Yuyuantan area as reference points to obtain the spatiotemporal distribution of land subsidence in the Beijing Plain. A total of 161575 PS points were identified.

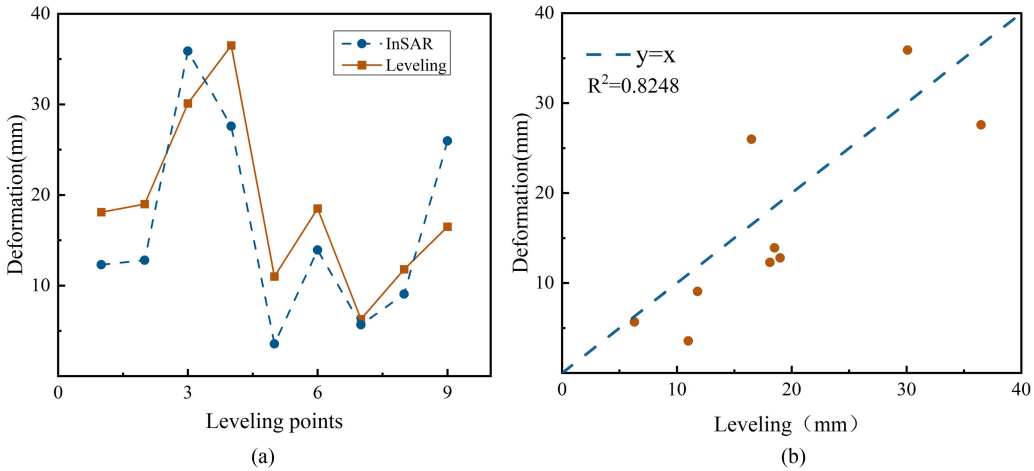


Fig. 5. Verification of the accuracy of the InSAR results. (a) Comparison of the deformation obtained by InSAR and leveling measurement data. (b) Linear fitting between the InSAR results and leveling measurement data.

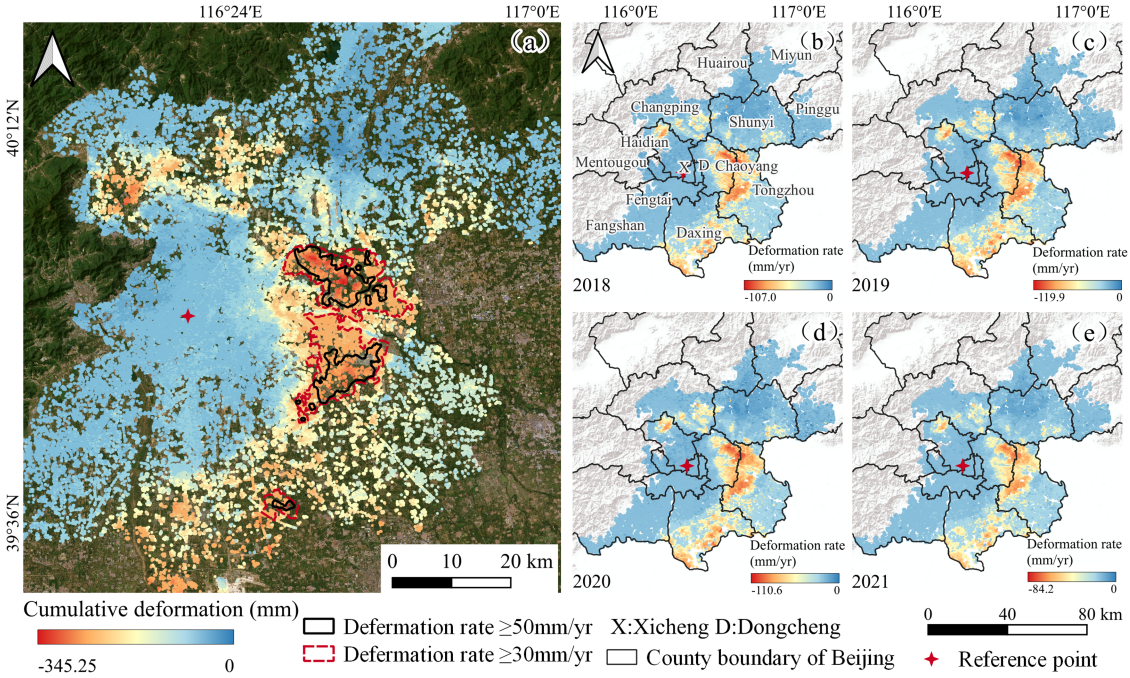


Fig. 6. (a) Annual average deformation rate on the Beijing Plain from January 2018 to August 2021. (b)–(e) Spatial evolution map of cumulative land subsidence from 2018 to 2021.

The spatial distribution varied greatly [see Fig. 6(a)]. The most severe land subsidence funnel was situated at the settlement centers of Jinzhan and Songzhuang. Between 2018 and 2021, the maximum cumulative settlement increased from 107 mm in 2018 to 345.25 mm in 2021, occurring at the settlement center of Songzhuang in the Tongzhou area, where the compressible layer is relatively thick [see Fig. 6(a)]. From 2018 to 2021, the maximum annual settlement decreased from 108 mm/yr in 2018 to 84.2 mm/yr in 2021, and the average annual settlement rate shows a trend of slowing down year by year. Although the maximum annual settlement rate increased from 107 mm/yr to 119.9 mm/yr in 2018–2019, the maximum annual settlement rates decreased to 110.6 mm/yr and 84.2 mm/yr in 2020 and 2021, respectively [see Fig. 6(b)–(e)].

According to the classification table of the land subsidence development degree (Table III) in the Code for Risk Assessment of Geological Hazards (GB_T 40112-2021) [35], we adopted annual settlement values of 30 and 50 mm as boundary values for dividing the land subsidence risk. Areas with an annual settlement higher than 30 mm were collectively referred to as serious settlement areas, and areas with an annual settlement higher than 50 mm were referred to as center settlement areas. As shown in Fig. 6(a), the areas with relatively serious settlements were mainly distributed in Chaoyang, Tongzhou, and Daxing Districts. Taihu town and Jinzhan and Songzhuang Districts

TABLE III
GRADING OF LAND SUBSIDENCE DEVELOPMENT

| Degree of development | Average settlement rate over the past 5 years (mm/yr) | Cumulative settlement (mm) |
|---|---|---|
| **Strong development** | ≥30 | ≥800 |
| **Moderate development** | 10–30 | 300–800 |
| **Weak development** | ≤10 | ≤300 |

Note: Only one of the above two factors can be met and determined in descending order.

TABLE IV
STATISTICAL ANALYSIS AND TEST RESULTS OF THE MGWR MODEL COEFFICIENTS

| Independent variable | Average | Maximum | Minimum | Median | Proportion of positive values (%) | Proportion of negative values (%) |
|---|---|---|---|---|---|---|
| UA | 0.063 | 1.678 | −0.977 | −0.008 | 49.33 | 50.67 |
| FCA | 0.153 | 4.793 | −2.968 | 0.138 | 57.46 | 42.54 |
| SCA | −0.080 | 8.796 | −7.470 | 0.033 | 54.51 | 45.49 |
| TCA | 0.03 | 8.089 | −4.632 | 0.025 | 42.70 | 57.30 |

exhibited the most serious settlement, with settlement rates higher than 50 mm/yr.

### B. Model Results and Assessment

*1) Spatial Autocorrelation:* Before MGWR analysis, spatial autocorrelation analysis in each independent variable (water head changes in UA, FCA, SCA, and TCA) and the cumulative land subsidence is required to ensure that the regression model could be established. This article calculates that Moran's I values of each variable are above 0.9, indicating significant spatial autocorrelation for each variable.

*2) MGWR Results and Assessment:* The MGWR model was constructed, and the statistical results of the regression coefficient between each aquifer and land subsidence are provided in Table IV.

The regression coefficient and average, minimum, maximum, and median values of each influencing factor were calculated, and the proportions of positive and negative regression coefficient values between each explanatory variable and land subsidence were calculated. The results indicated that various influencing factors have both negative and positive effects on land subsidence. The FCA attained the highest ratio of positive coefficient values (57.46%), and TCA attained the highest ratio of negative coefficient values (57.3%). The MGWR model yielded a specific regression coefficient for each grid in the calculation results.

### C. Correlation Between the Water Head Change in Different Aquifer Groups and Land Subsidence Based on the MGWR Model

*1) Spatial Heterogeneity of the Regression Coefficient Between Land Subsidence and the Water Head Change of Each Aquifer Group:* The regression coefficients of various influencing factors obtained by the MGWR model vary in size. We normalize and classify coefficients to compare correlations on the same order of magnitude. The normalized regression coefficients ranged from −1 to 1, boundary values of −0.3 and 0.3 were selected, and finally, the normalized regression coefficients were divided into four categories: −1–0.3, −0.3–0, 0–0.3, and 0.3–1.

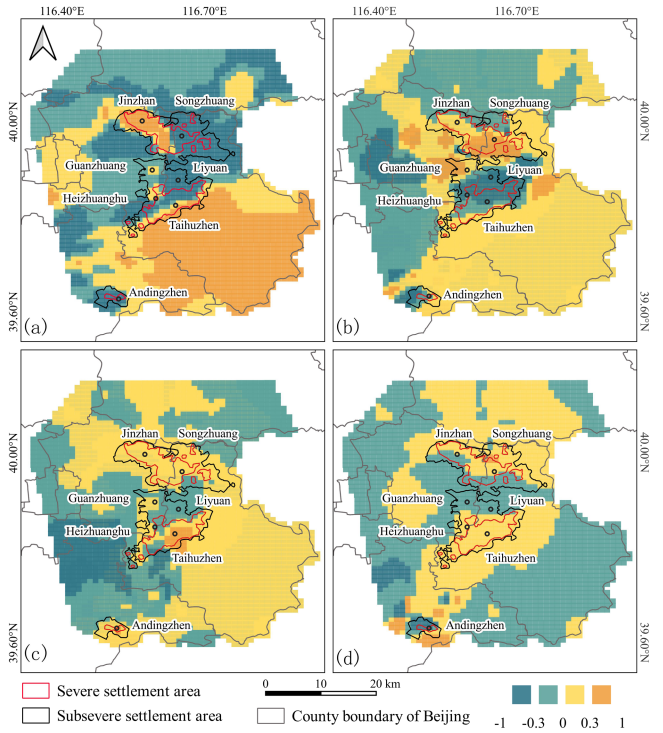


Fig. 7. Spatial heterogeneity map of the relationship between land subsidence and groundwater change. Spatial distribution of (a) UA, (b) FCA, (c) SCA, and (d) TCA regression coefficients.

There were spatial differences in the influence of the different aquifers on land subsidence. The distribution diagram of the correlation coefficient between the groundwater head change and land subsidence is shown in Fig. 7. In the serious settlement area, the correlation between the groundwater head change in the UA and land subsidence was negative in most areas, which may be due to the notable effect of rainfall and other external factors on the recharge to groundwater process of the UA, resulting in large groundwater head fluctuations. The area proportion of positive regression coefficient values between the water head change in the FCA and land subsidence was lower than that between the groundwater head change in the SCA and TCA and land subsidence. The regression coefficients of the SCA were positive in almost all areas, and the correlation with groundwater change was the highest. The SCA contributed the most to subsidence. The positive regression coefficient values of the TCA were also higher in the serious subsidence area, and the aquifer imposed an obvious positive effect on land subsidence. Therefore, overexploitation of the second and third confined aquifers greatly promoted land subsidence in the serious subsidence areas.

*2) Contribution Degree of the Water Head Changes in Aquifer Groups to Land Subsidence:* According to (4), in the serious settlement areas, the contribution rate of each aquifer to

TABLE V
COMPRESSION RATIO OF DIFFERENT LAYERS

| | UA | FCA | SCA | TCA |
|---|---|---|---|---|
| **Results of this article** | 14.75% (0–50 m) | 23.65% (50–100 m) | 33.44% (100–180 m) | 28.16% (>180 m) |
| **Baxianzhuang** | 11.08% (2–59 m) | 54.38%(59–144 m) | | 34.54% (>144 m) |

land subsidence was estimated in areas with positive correlation coefficients between the water head change in the different aquifer groups and land subsidence.

The contribution of the UA is 14.75% and that of the FCA is 23.65%. The contribution of the SCA is 33.44% and that of the TCA is 28.16%. Based on these findings, the contribution rate is taken as the settlement proportion of different compression layer groups, which agrees with the extensometer deformation results of Baxianzhuang of Lei Kunchao [26] (Table V). The SCA yielded the highest contribution, followed by the TCA, while the UA yielded the lowest contribution. Most groundwater exploitation in Beijing occurs within 200 m, mainly concentrated in the FCA and SCA, and thus, the contribution of the SCA is high, but the top half of the TCA is also the main exploitation layer for domestic and industrial water in these regions.

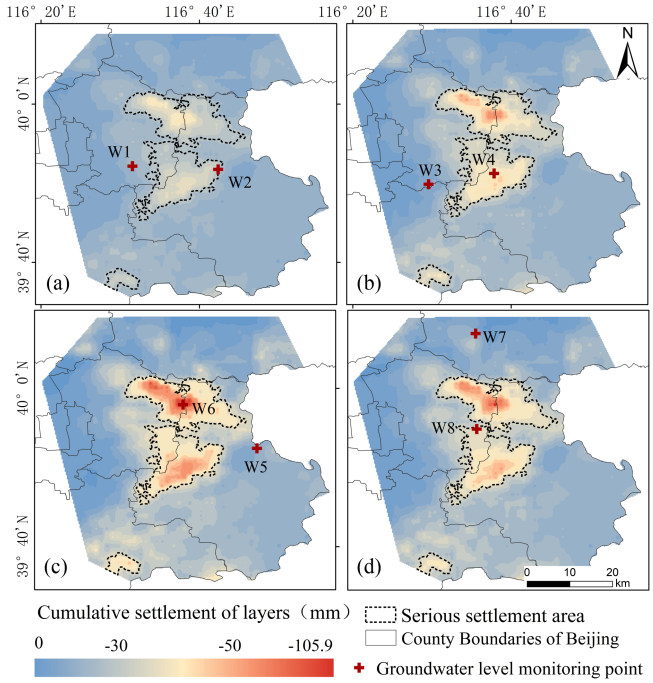


Fig. 8. Spatial distribution of the cumulative settlement of the four-layered aquifer groups from 2018 to 2021 and groundwater head monitoring points. Spatial pattern of the cumulative settlement of (a) UA, (b) FCA, (c) SCA, and (d) TCA.

### *D. Deformation Characteristics of the Different Aquifer Groups Under Different Water Head Change Modes*

According to the settlement results for Beijing obtained via PS-InSAR technology mentioned earlier, the settlement proportions of different compression layer groups were 14.75%, 23.65%, 33.44%, and 28.16%. The cumulative settlement from 2018 to 2021 was decomposed into different aquifers. The figure shows that the settlement of the SCA was the greatest. In the study area, long-term groundwater head monitoring wells at different depths were selected inside and outside the serious subsidence area (see Fig. 8). Adopting the monitoring well as the center of the buffer zone, the mean land settlement value of the different aquifers and the corresponding groundwater head change value during the same period in the buffer zone were obtained, and the stress–strain diagram was used to analyze the soil deformation characteristics under the various modes of water head change.

Based on groundwater and settlement data, the deformation characteristics of soil can be divided into three types: elastic, elastic-inelastic, and inelastic (see Fig. 9). W1, W3, and W7 mainly exhibited elasto-plastic deformation. The residual deformation was large, including plastic and creep deformation. Numerous hysteresis loops can be recognized in the stress–strain curve. W5 largely indicated elastic deformation. This result is related to the lithology of the multiple sand layers. The sand layers were compacted due to the decrease in the pore-water pressure. After the pore-water pressure was restored, the sand layers generally recovered their original states [36]. W2, W4, W6, and W8 mainly indicated plastic deformation. The observed settlement always indicated a state of continuous subsidence, with large residual deformation and hysteresis phenomena.

Stress–strain curves of monitoring wells under different water head change modes are shown. The different subsidence areas and lithologies exhibited different deformation characteristics. Outside the serious subsidence area, the deformation characteristics of both shallow and deep soil layers mainly indicate elastic and elastoplastic deformation. In the serious settlement area, the deformation characteristics of the shallow soil mass largely indicated plastic deformation, but in 2020, the groundwater head increased, and elastic deformation characteristics could be observed. The deformation characteristics of the deep soil mass mainly included plastic deformation. Overall, the deformation characteristics of the soil mass at the monitoring well outside the serious subsidence area mainly indicated elastic deformation, while inside the serious subsidence area at the monitoring well mainly indicated plastic deformation. However, some monitoring wells did not conform to this rule, which mainly occurred because the deformation characteristics of the soil mass are primarily determined by the joint effects of the lithology and groundwater head change mode.

The deformation characteristics of the various soil masses with varying lithology differed. In these eight monitoring well areas, two water wells within the same layer are compared: in areas with a high proportion of water-bearing sand layers, the soil deformation features mostly indicated elastic deformation, and the surface deformation and water head change were basically synchronous. When the water head recovered or the downward trend of the water head declined, the settlement rebounded or

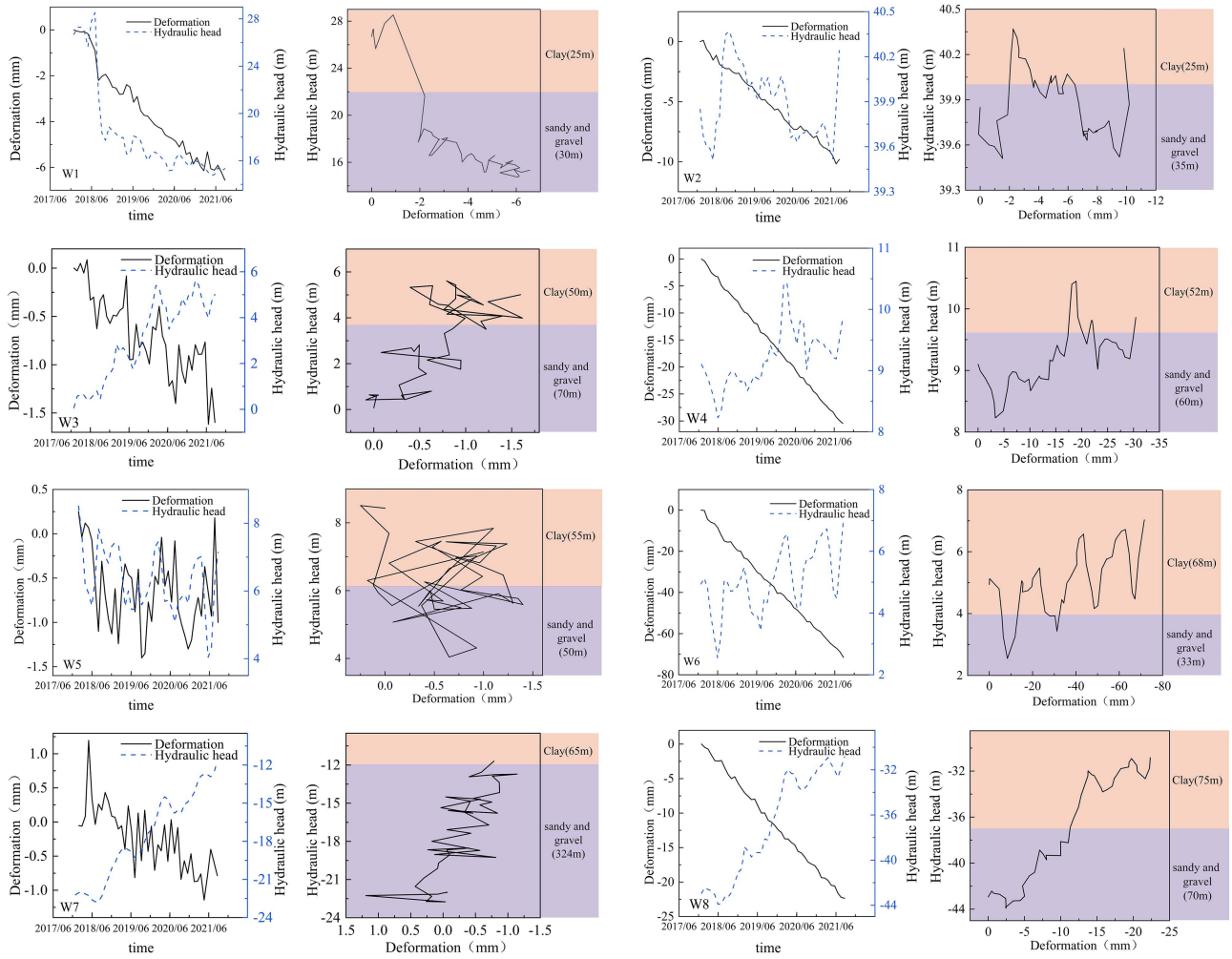


Fig. 9. Correlation curve between settlement and groundwater variation (left figure) and stress–strain curve of settlement due to groundwater variation (right figure) of eight monitoring wells. (The purple and pink backgrounds indicate the thicknesses of the water-bearing sand layer and aquitard layer, respectively, at the well location).

was absent. In areas with a low proportion of water-bearing sand layers, the soil deformation characteristics mainly suggested plastic deformation, with significant residue deformation and deformation hysteresis. When the water head rapidly increased or the declining trend of the water head decreased, the settlement did not rebound or the rebound amount was very small. The large residual deformation mainly occurred because the plastic storage coefficient was 1–2 orders of magnitude higher than the elastic storage coefficient. The deformation lag was largely due to the dissipation of redundancy pore-water pressure in the weakly permeable zone occurring after the groundwater head change.

## V. Discussion

### A. Comparison of the Storage Values

According to Section IV, the settlement proportions of different compression layer groups were 14.75%, 23.65%, 33.44%, and 28.16%. The cumulative settlement value of each aquifer layer from 2018 to 2021 was calculated, and the groundwater head change data were superimposed (see Fig. 10).

According to (6), the water storage coefficient of the 1 km × 1 km grid of different aquifer skeletons could be obtained by using the cumulative settlement data of the different layers and the water head change data of each layer (see Fig. 10). The spatial distribution ranges of the UA, FCA, SCA, and TCA skeletal water storage coefficients were defined according to the boundary of each aquifer group, as shown in Fig. 2(a).

Numerous studies have shown that the theoretical value of the elastic storage coefficient varies between $n\times10^{-5}$ and $n\times10^{-3}$. In aquifers mainly composed of loose clay and silt, the inelastic water storage coefficient is 1–2 orders of magnitude higher than the elastic storage coefficient [1], [18], [37], [38].

The range of storage coefficient values for UA is $0.002\times10^{-3}-641.58\times10^{-3}$. The range of storage coefficient values for FCA is $0.003\times10^{-3}-806.18\times10^{-3}$. The range of storage coefficient values for SCA is $0.005\times10^{-3}-484.58\times10^{-3}$. The range of storage coefficient values for TCA is $0.003\times10^{-3}-608.7\times10^{-3}$. The calculated water storage coefficient values conformed to the theoretical storage coefficient values.

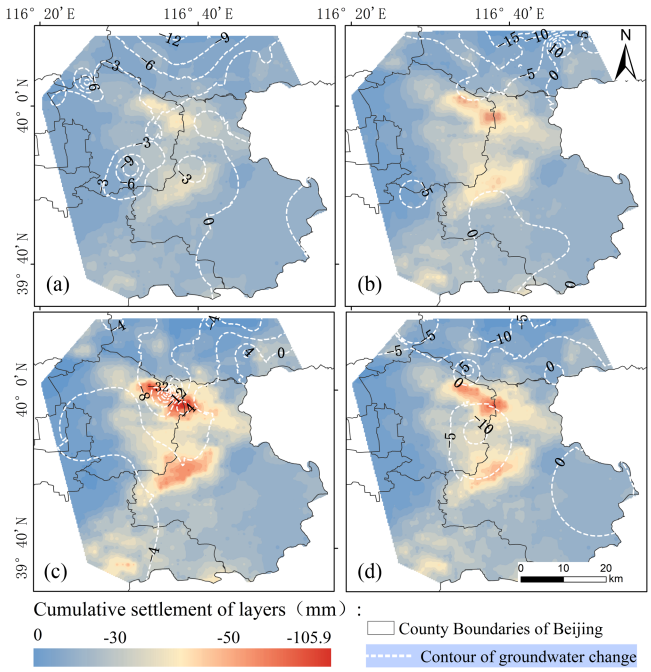


Fig. 10. Spatial pattern of the cumulative settlement of the different aquifers and contours of the groundwater head buried depth change from 2018 to 2021: Spatial distribution of the cumulative settlement and head change isopleth of (a) UA, (b) FCA, (c) SCA, and (d) TCA.

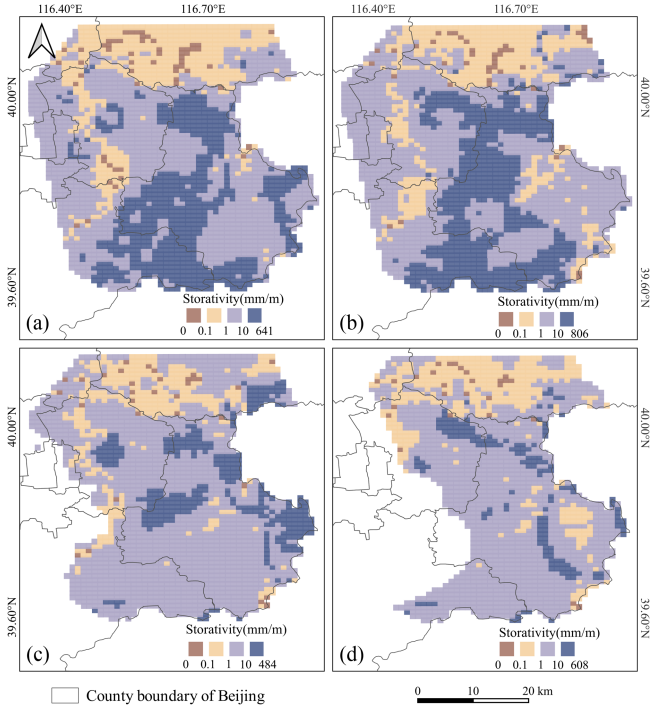


Fig. 11. Spatial pattern of the water storage coefficients: Spatial pattern of (a) UA, (b) FCA, (c) SCA, and (d) TCA skeletal storage coefficients.

We found that the water storage coefficients of different aquifer groups exhibit different spatial distribution characteristics, which is due to the different lithological compositions and groundwater exploitation of different aquifers. The water storage coefficient of the elastic skeleton roughly shows a trend of increasing from north to south and from west to east, which is related to the seasonal fluctuations in the aquifer thickness and groundwater level in the Beijing Plain. The water storage coefficient of the inelastic skeleton is mainly distributed in areas with relatively thick compressible layers and a significant decrease in the groundwater level.

The distribution range of elastic skeleton water storage coefficients in different aquifer groups is very similar, with a small number of areas (brown and yellow) having values of $n\times10^{-4}$, which is the typical storage coefficient of elastic skeleton structures, representing elastic deformation, located in the north and west of the study area. The distribution characteristics of the inelastic skeleton water storage coefficient have significant differences: for inelastic skeleton water storage coefficients greater than $10\times10^{-3}$, the distribution is wider in UA and FCA, while the distribution range of SCA and TCA is smaller (see Fig. 11). The spatial distribution range of aquifer water storage coefficients greater than $10\times10^{-3}$ (dark purple) is consistent with that of the serious settlement area. In most regions (light purple), the value is $n\times10^{-3}$, which is the typical water storage coefficient of inelastic skeleton structures, indicating that most soil deformation characteristics in the study area entail inelastic deformation, primarily distributed in areas with settlement development.

TABLE VI
SUMMARY OF THE AVERAGE WATER STORAGE COEFFICIENT OF EACH AQUIFER LAYER

| Aquifer Group | $S_{ke}$ | $S_{kv}$ |
|---|---|---|
| **UA** | $0.44\times10^{-3}$ | $17.47\times10^{-3}$ |
| **FCA** | $0.48\times10^{-3}$ | $14.65\times10^{-3}$ |
| **SCA** | $0.5\times10^{-3}$ | $7.98\times10^{-3}$ |
| **TCA** | $0.57\times10^{-3}$ | $7.94\times10^{-3}$ |

### *B. Storage Value Change With Depth*

To characterize the water storage coefficient variation with the depth of the different aquifer systems, the average $S_{ke}$ and $S_{kv}$ values of the different aquifers were calculated (Table VI). For $S_{ke}$, from the shallow layer $0.44\times10^{-3}$ increase to the deep $0.57\times10^{-3}$, and for $S_{kv}$, from the shallow layer $17.47\times10^{-3}$ decrease to the deep $7.94\times10^{-3}$.

As shown in Fig. 11, the brown and yellow areas indicate the spatial distributions of the elastic water storage coefficient. The elastic water storage coefficient of the medium-deep aquifer layer was higher than that of the shallow and first confined aquifers. This finding suggests that the elastic storage capacity of the medium-deep aquifer layer is higher than that of the other aquifer layers. We usually consider that elastic water storage mainly occurs in the water-bearing sand layer. According to the profile shown in Fig. 2(c) and the hydrogeological profile of the Beijing Plain obtained by Lei Kunchao et al., it could be speculated that this occurs because the thickness of the medium-deep aquitard layer is larger than that of the shallow layer, the corresponding hydrodynamic delay time is longer,

TABLE VII
COMPARISON OF THE AQUIFER DEFORMATION CHARACTERISTICS AND $S_K$ AMONG THE DIFFERENT MONITORING WELLS

| Monitoring well | Lithology | Sand/clay ratio | Buried depth (m) | Deformation characteristics | $S_k$ |
|---|---|---|---|---|---|
| **W1** | Sand, silty clay | 1.2 | 34 | Elastic-inelastic | $0.53\times10^{-3}$ |
| **W2** | Sand, silty clay | 1.4 | 47 | Inelastic | $26.77\times10^{-3}$ |
| **W3** | Sand, silty clay | 1.4 | 100 | Elastic-inelastic | $0.12\times10^{-3}$ |
| **W4** | Sand, silty clay | 1.15 | 80 | Inelastic | $51.61\times10^{-3}$ |
| **W5** | Sand, silty clay | 0.9 | 124 | Elastic | $0.1\times10^{-3}$ |
| **W6** | Clay | 0.48 | 121 | Inelastic | $44.25\times10^{-3}$ |
| **W7** | Sand | 4.98 | 250 | Elastic-inelastic | $0.46\times10^{-3}$ |
| **W8** | Sand, silty clay | 0.9 | 200 | Inelastic | $2.83\times10^{-3}$ |

the water level greatly decreases, the effective stress notably increases, and the corresponding water release volume of the water-bearing sand layer is large. In contrast, if the shallow aquitard is relatively thin, the aquifer recharge process is fast, the hydrodynamic delay time is short, the aquifer water pressure changes slightly, and the effective stress increases slightly. Then, the compression-related water release volume of the aquifer sand layer is small.

The light and dark purple areas indicate the spatial distributions of the inelastic water storage coefficient, most of which occur in areas with serious settlement. Regarding the inelastic water storage coefficient, the value of the middle-deep aquifer was lower than that of the shallow aquifer (Table VI). We usually consider that inelastic water release mainly originates from the aquitard. The inelastic water storage coefficient of the deep aquifer is lower than that of the shallow aquifer because the thickness of the deep clay layer is larger than that of the shallow layer, the water release process of the clay layer is relatively slow, the hydrodynamic delay time is longer, and the compression-related water release volume of the clay layer decreases when the unit head declines. In contrast, when the shallow aquitard is relatively thin, the hydrodynamic delay time is short, and the compression-related water release volume of the clay layer is large under a unit head drop. In addition, the soil layer inelastic compaction is irrecoverable. Previous studies have demonstrated that the permeability coefficient, $S_{ke}$, $S_{kv}$, and related specific values ($S_{ske}$ and $S_{skv}$, respectively) decrease with a permanent drop in the water level [39], [40]. Land subsidence in the Beijing Plain has appeared since the 1950s, and the compaction of the middle-deep clay layer is the most serious. Therefore, the long-term compaction of the clay layer may also explain the smaller $S_{kv}$ value of the middle-deep aquifer than that of the shallow aquifer and the FCA. This result further indicates that with continuous settlement development in the Beijing Plain, the storage performance of the aquifer group declines, and the decline range of the middle-deep layer is greater than that of the shallow layer.

### C. Relationship Between the Storage Value and Lithology

The relationship between the lithology and water storage coefficient was analyzed by comparing the soil deformation characteristics at the different monitoring well locations and the water storage coefficient values in the corresponding areas. Comparing the results of two monitoring wells in the same aquifer layer, it is shown that when the ratio of sand to clay is high, the deformation characteristics of the soil in the monitoring well area mainly involve elastic deformation, and the storage coefficient is that of $S_{ke}$ (Table VII). When the ratio of sand to clay is low, the soil deformation characteristics at the monitoring well sites mainly suggest inelastic deformation, and the water storage coefficient is $S_{kv}$. For example, regarding W6, the lithology is mainly clay, the deformation characteristics of the soil mass suggest inelastic deformation, and the inelastic water storage coefficient is $44.25\times10^{-3}$.

The deformation characteristics of the soil mass are primarily determined by the joint effects of the lithology and groundwater head change mode. For specific monitoring well W2, the ratio of sand to clay is relatively high, but the soil layer deformation characteristics mainly indicated inelastic deformation, and the water storage coefficient was inelastic. Although the thickness of the water-bearing sand layer is greater than that of the clay layer, based on the clay layer with a certain thickness, due to the notable decline in the water head at the early stage, the scatter and disappearance of redundancy pore water pressure in the aquifer lags significantly behind the groundwater variation. Therefore, the deformation characteristics of the W2 soil layer indicated inelastic deformation, and the water storage coefficient was the same as that of the inelastic skeleton. The ratio of sand to clay in well W5 was relatively low, but the soil layer deformation characteristics mainly indicated elastic deformation, and the water storage coefficient was elastic. Based on the stress–strain analysis of the W5 well (see Fig. 9), the average annual water level change remains basically unchanged, and most of the wells are located in the water-bearing sand layer. Although the ratio of sand to clay is small, the effective stress of the soil does not increase under the condition of small annual water level changes, and well W5 exhibits elastic deformation characteristics.

### D. Advantages and Limitations of the Framework

In this study, we proposed a new research framework that combines the PS-InSAR method and MGWR model to obtain land subsidence data for different aquifer groups and then invert

the water storage coefficients of different aquifer groups. The advantage of this framework is that it can obtain settlement data of spatial scale stratification in the absence of layered standard data, which can then invert the water storage coefficient of spatial scale stratification.

Note that when using this framework to estimate the water storage coefficient, we assume that the water storage coefficient is constant throughout the entire study period (2018–2021). Generally, this assumption is reasonable in our study, particularly for most areas that have experienced significant land subsidence. However, due to the large number of PS points and the limitations of the MGWR model on the amount of input data, we adopted a $1 \times 1$ km grid to serve as the input sample points for the model, reducing the number of sample points while preserving the original geographic feature information. This usually leads to changes in the value of the water storage coefficient. In the future, with the improvement of the algorithm, we can use the ps point as the input point of the sample model to obtain more accurate results. In addition, this article did not consider the differences in hydrogeological conditions in different regions. In the whole study area, we use the same settlement compression ratio. In future research, we will consider the hydrogeological conditions of different regions for zoning, obtain the layered settlement compression ratio in different regions, and estimate the water storage coefficient.

## VI. Conclusion

The long-term development of land subsidence in Beijing has resulted in the loss of aquifer storage capacity. A research framework has been proposed that combines PS-InSAR technology with spatial correlation models to obtain settlement information and water storage coefficients of different aquifer groups. This framework was applied to the Beijing Plain area to examine the deformation characteristics of various soil masses under various water head variation modes, retrieve the water storage coefficient of different aquifers at the spatial scale, and evaluate the water storage characteristics of different aquifer groups.

The research results indicate that the main factors influencing land subsidence in the two major settlement funnels were the FCA, SCA and TCA, and the settlement proportions of the different compression layer groups were 14.75%, 23.65%, 33.44%, and 28.16%, respectively. The range of water storage coefficients for phreatic water and the first, second, and third confined aquifers is between $0.002\times10^{-3}-641.58\times10^{-3}$, $0.003\times10^{-3}-806.18\times10^{-3}$, $0.005\times10^{-3}-484.58\times10^{-3}$ and $0.003\times10^{-3}-608.7\times10^{-3}$, respectively. The water storage coefficient of the elastic skeleton roughly shows a trend of increasing from north to south and from west to east, which is related to the seasonal fluctuations in the aquifer thickness and groundwater level in the Beijing Plain. The water storage coefficient of the inelastic skeleton is mainly distributed in areas with relatively thick compressible layers and a significant decrease in the groundwater level.

With the continuous development of subsidence, the water storage performance of the aquifer group is continuously declining. These findings contribute to managing the sustainable use of groundwater resources and controlling subsidence. It is demonstrated that the research framework proposed in this article can serve as an effective tool for obtaining settlement information and the skeleton water storage coefficient of different aquifer groups.

## Acknowledgment

The authors would like to thank the Hydrological and Water Resources Monitoring and Evaluation Center of the Ministry of Water Resources of China and the relevant departments of the China Geological Environment Monitoring Institute for providing data support and verification.

## References

[1] D. L. Galloway and T. J. Burbey, "Review: Regional land subsidence accompanying groundwater extraction," *Hydrogeol. J.*, vol. 19, no. 8, pp. 1459–1486, 2011, doi: 10.1007/s10040-011-0775-5.

[2] G. Herrera-García et al., "Mapping the global threat of land subsidence," *Science*, vol. 371, no. 6524, pp. 34–36, 2021, doi: 10.1126/science.abb8549.

[3] M. M. Miller and M. Shirzaei, "Land subsidence in Houston correlated with flooding from Hurricane Harvey," *Remote Sens. Environ.*, vol. 225, pp. 368–378, 2019, doi: 10.1016/j.rse.2019.03.022.

[4] A. Rezaei and Z. Mousavi, "Characterization of land deformation, hydraulic head, and aquifer properties of the Gorgan confined aquifer, Iran, from InSAR observations," *J. Hydrol.*, vol. 579, 2019, Art. no. 124196, doi: 10.1016/j.jhydrol.2019.124196.

[5] T. T. Thoang and P. H. Giao, "Subsurface characterization and prediction of land subsidence for HCM city, Vietnam," *Eng. Geol.*, vol. 199, pp. 107–124, 2015, doi: 10.1016/j.enggeo.2015.10.009.

[6] H. Gong et al., "Long-term groundwater storage changes and land subsidence development in the north China Plain (1971–2015)," *Hydrogeol. J.*, vol. 26, no. 5, pp. 1417–1427, 2018, doi: 10.1007/s10040-018-1768-4.

[7] L. Hu et al., "Land subsidence in Beijing and its relationship with geological faults revealed by Sentinel-1 InSAR observations," *Int. J. Appl. Earth Observ. Geoinformation*, vol. 82, 2019, Art. no. 101886, doi: 10.1016/j.jag.2019.05.019.

[8] Y. Zhang, H. Gong, Z. Gu, R. Wang, X. Li, and W. Zhao, "Characterization of land subsidence induced by groundwater withdrawals in the Plain of Beijing City, China," *Hydrogeol. J.*, vol. 22, no. 2, pp. 397–409, 2014, doi: 10.1007/s10040-013-1069-x.

[9] A. Rezaei, M. Zare, and H. Zhan, "Aquitard horizontal dispersion on reactive solute transport in an aquifer–aquitard system," *Transport Porous Media*, vol. 113, no. 3, pp. 695–716, 2016, doi: 10.1016/j.advwatres.2013.08.013.

[10] A. Ferretti, A. Fumagalli, F. Novali, C. Prati, F. Rocca, and A. Rucci, "A new algorithm for processing interferometric data-stacks: SqueeSAR," *IEEE Trans. Geosci. Remote Sens.*, vol. 49, no. 9, pp. 3460–3470, Sep. 2011, doi: 10.1109/TGRS.2011.2124465.

[11] Q. Yang et al., "Multi-scale analysis of the relationship between land subsidence and buildings: A case study in an eastern Beijing urban area using the PS-InSAR technique," *Remote Sens.*, vol. 10, no. 7, 2018, Art. no. 562, doi: 10.3390/rs10071006.

[12] H. Li et al., "Spatiotemporal modeling of land subsidence using a geographically weighted deep learning method based on PS-InSAR," *Sci. Total Environ.*, vol. 799, 2021, Art. no. 149244, doi: 10.1016/j.scitotenv.2021.149244.

[13] H. Li et al., "Land subsidence due to groundwater pumping: Hazard probability assessment through the combination of Bayesian model and fuzzy set theory," *Natural Hazards Earth Syst. Sci.*, vol. 21, no. 2, pp. 823–835, 2021, doi: 10.5194/nhess-21-823-2021.

[14] D. L. Galloway and J. Hoffmann, "The application of satellite differential SAR interferometry-derived ground displacements in hydrogeology," *Hydrogeol. J.*, vol. 15, no. 1, pp. 133–154, 2007, doi: 10.1007/s10040-006-0121-5.

[15] J. W. Bell et al., "Permanent scatterer InSAR reveals seasonal and long-term aquifer-system response to groundwater pumping and artificial recharge," *Water Resour. Res.*, vol. 44, no. 2, 2008, Art. no. 215025, doi: 10.1029/2007WR006152.
[16] R. Bonì, F. Cigna, S. H. Bricker, C. Meisina, and H. McCormack, "Characterisation of hydraulic head changes and aquifer properties in the London Basin using Persistent Scatterer Interferometry ground motion data," *J. Hydrol.*, vol. 540, pp. 835–849, 2016, doi: 10.1016/j.jhydrol.2016.06.068.
[17] E. Chaussard, R. Bürgmann, M. Shirzaei, E. J. Fielding, and B. Baker, "Predictability of hydraulic head changes and characterization of aquifer-system and fault properties from InSAR-derived ground deformation," *J. Geophysical Res.: Solid Earth*, vol. 119, no. 8, pp. 6572–6590, 2014, doi: 10.1002/2014JB011266.
[18] J. Hoffmann, H. A. Zebker, D. L. Galloway, and F. Amelung, "Seasonal subsidence and rebound in Las Vegas Valley, Nevada, observed by synthetic aperture radar interferometry," *Water Resour. Res.*, vol. 37, no. 6, pp. 1551–1566, 2001, doi: 10.1029/2000WR900404.
[19] X. Hu, Z. Lu, and T. Wang, "Characterization of hydrogeological properties in Salt Lake Valley, Utah, using InSAR," *J. Geophysical Res.: Earth Surf.*, vol. 123, no. 6, pp. 1257–1271, 2018, doi: 10.1029/2017JF004497.
[20] L. Jiang et al., "Combining InSAR and hydraulic head measurements to estimate aquifer parameters and storage variations of confined aquifer system in Cangzhou, North China Plain," *Water Resour. Res.*, vol. 54, no. 10, pp. 8234–8252, 2018, doi: 10.1029/2017WR022126.
[21] X. Zhang et al., "Inversion of groundwater storage variations considering lag effect in Beijing Plain, from RadarSat-2 with SBAS-InSAR technology," *Remote Sens.*, vol. 14, 2022, Art. no. 991, doi: 10.3390/rs14040991.
[22] B. Riel, M. Simons, D. Ponti, P. Agram, and R. Jolivet, "Quantifying ground deformation in the Los Angeles and Santa Ana coastal basins due to groundwater withdrawal," *Water Resour. Res.*, vol. 54, no. 5, pp. 3557–3582, 2018, doi: 10.1029/2017WR021978.
[23] F. S. Riley, *Analysis of Borehole Extensometer Data From Central California*. Paris, France: UNESCO, 1970.
[24] L. Bai et al., "Quantifying the influence of long-term overexploitation on deep groundwater resources across Cangzhou in the North China Plain using InSAR measurements," *J. Hydrol.*, vol. 605, 2021, Art. no. 127368, doi: 10.1016/j.jhydrol.2021.127368.
[25] J. Li et al., "Unraveling elastic and inelastic storage of aquifer systems by integrating fast independent component analysis and a variable preconsolidation head decomposition method," *J. Hydrol.*, vol. 606, 2022, Art. no. 127420, doi: 10.1016/j.jhydrol.2021.127420.
[26] K. Lei et al., "Main subsidence layers and deformation characteristics in Beijing Plain at present," *J. Eng. Geol.*, vol. 30, no. 2, pp. 442–458, 2022, doi: 10.13544/j.cnki.jeg.2021-0238.
[27] A. Zhang, *Groundwater in Beijing*. Beijing, China: Land Press, 2008.
[28] A. Ferretti, C. Prati, and F. Rocca, "Nonlinear subsidence rate estimation using permanent Scatterers in differential SAR interferometry," *IEEE Trans. Geosci. Remote Sens.*, vol. 38, no. 5, pp. 2202–2212, Sep. 2000, doi: 10.1109/36.868878.
[29] D. Perissin, Z. Wang, and H. Lin, "Shanghai subway tunnels and highways monitoring through Cosmo-SkyMed Persistent Scatterers," *ISPRS J. Photogrammetry Remote Sens.*, vol. 73, pp. 58–67, 2012, doi: 10.1016/j.isprsjprs.2012.07.002.
[30] L. Q. Guo, W. Bo, and G. H. Yang, "Characteristics of current deformation of fault belts in North China," *J. Geodesy Geodynamics*, vol. 23, no. 2, pp. 29–36, 2003.
[31] A. Fotheringham, W. Yang, and W. Kang, "Multiscale geographically weighted regression (MGWR)," *Ann. Amer. Assoc. Geographers*, vol. 107, no. 6, pp. 1247–1265, 2017, doi: 10.1080/24694452.2017.1352480.
[32] R. J. M. De Wiest, "On the storage coefficient and the equations of groundwater flow," *J. Geophysical Res.*, vol. 71, no. 4, pp. 1117–1122, 1966, doi: 10.1029/JZ071i004p01117.
[33] M. O. Saar and M. Manga, "Seismicity induced by seasonal groundwater recharge at Mt. Hood, Oregon," *Earth Planet. Sci. Lett.*, vol. 214, no. 3, pp. 605–618, 2003, doi: 10.1016/S0012-821X(03)00418-7.
[34] L. Bai, Z. Li, S. Song, and D. Liu, "Estimation of the land deformation and aquifer parameters in the Handan Plain using multitemporal InSAR technology," *Chin. J. Geophys.*, vol. 65, no. 09, pp. 3351–3362, 2022, doi: 10.6038/cjg2022P0845.
[35] Yueping Yin, "Specifications for Risk Assessment of Geological Hazard." China Standard Publishing House, China: Yueping Yin, 2021.
[36] L. Liu, *Foundation of Hydrogeology*. Beijing, China: Land Press, 2008.
[37] D. L. Galloway et al., "Detection of aquifer system compaction and land subsidence using interferometric synthetic aperture radar, Antelope Valley, Mojave Desert, California," *Water Resour. Res.*, vol. 34, no. 10, pp. 2573–2585, 1998, doi: 10.1029/98WR01285.
[38] J. Hoffmann, D. L. Galloway, and H. A. Zebker, "Inverse modeling of interbed storage parameters using land subsidence observations, Antelope Valley, California," *Water Resour. Res.*, vol. 39, no. 2, 2003, Art. no. 25102, doi: 10.1029/2001WR001252.
[39] Z. Li, Z. Zhou, M. Li, and Z. Cuiying, "Variation of hydraulic parameters of aquitard during water release," *J. Hohai Univ.*, vol. 45, no. 4, pp. 340–344, 2017, doi: 10.3876/j.issn.1000-1980.2017.04.009.
[40] R. Liu, G. Cao, and Y. Zhao, "A study of the influence of land subsidence on hydraulic parameters and water supply capacity," *Hydrogeol. Eng. Geol.*, vol. 46, no. 3, pp. 47–54, 2019, doi: 10.16030/j.cnki.issn.1000-3665.2019.03.07.

**Danni Zhao** is currently working toward the master's degree with the Key Laboratory of the Ministry of Education Land Subsidence Mechanism and Prevention, College of Resources Environment and Tourism, Capital Normal University, Beijing, China.

Her research interests include using interferometric synthetic aperture radar technology to obtain regional land subsidence information and analyzing the response relationship between land subsidence and water level changes in layered aquifer groups.

**Beibei Chen** received the M.S. and Ph.D. degrees in cartography and geographic information systems from Capital Normal University, Beijing, China, in 2009 and 2012, respectively.

From 2012 to 2014, she was a Postdoctoral Fellow with the School of Mathematical Sciences, Capital Normal University. She is currently a Professor with the College of Resources Environment and Tourism, Capital Normal University. Her research interests include land subsidence and hydrogeology.

**Huili Gong** received the M.S. and Ph.D. degrees in hydrological geology and engineering geology from Changchun Geological College, Changchun, China, in 1993 and 1996, respectively.

From 1996 to 1998, he was a Postdoctoral with the Institute of Remote Sensing, Beijing University. He is currently a Professor with the College of Resources Environment and Tourism, Capital Normal University, Beijing, China, and also with the Key Laboratory of 3-D Information Acquisition and Application, Ministry of Education, Capital Normal University. He is with the Russian Academy of Engineering, Moscow, Russia. His research interests include land subsidence and hydrogeology.

**Kunchao Lei** received the master's degree in cartography and geographic information systems from Capital Normal University, Beijing, China, in 2011.

He is currently a Professor-Level Senior Engineer with the Geological Environment Monitoring Institute, Beijing, China. His research interests include regional land subsidence.

**Chaofan Zhou** received the Ph.D. degree in cartography and geographic information systems from Capital Normal University, Beijing, China, in 2018.

She is currently a Lecturer with the College of Resources Environment and Tourism, Capital Normal University. Her research interests include regional land subsidence.

**Jinming Hu** is currently working toward the master's degree with the Key Laboratory of the Ministry of Education Land Subsidence Mechanism and Prevention, College of Resources Environment and Tourism, Capital Normal University, Beijing, China.

His research interests include obtaining regional land subsidence information using interferometric synthetic aperture radar technology and constructing soil and water coupling models to predict the land subsidence caused by groundwater exploitation.